Controlling water evaporation through self-assembly

Kevin Roger, Marianne Liebi, Jimmy Heimdal, Quoc Dat Pham, Emma Sparr

Controlling water evaporation through self-assembly

Kevin Roger[a,b,1], Marianne Liebi[c], Jimmy Heimdal[d], Quoc Dat Pham[b], and Emma Sparr[b]

[a]Laboratoire de Génie Chimique, Université de Toulouse, CNRS, Institut National Polytechnique de Toulouse, Université Paul Sabatier, 31030 Toulouse, France; [b]Division of Physical Chemistry, Chemical Center, Lund University, SE-22100 Lund, Sweden; [c]Paul Scherrer Institut, 5232 Villigen PSI, Switzerland; and [d]MAX-IV Laboratory, Lund University, SE-22100 Lund, Sweden

Water evaporation concerns all land-living organisms, as ambient air is dryer than their corresponding equilibrium humidity. Contrarily to plants, mammals are covered with a skin that not only hinders evaporation but also maintains its rate at a nearly constant value, independently of air humidity. Here, we show that simple amphiphiles/water systems reproduce this behavior, which suggests a common underlying mechanism originating from responding self-assembly structures. The composition and structure gradients arising from the evaporation process were characterized using optical microscopy, infrared microscopy, and small-angle X-ray scattering. We observed a thin and dry outer phase that responds to changes in air humidity by increasing its thickness as the air becomes dryer, which decreases its permeability to water, thus counterbalancing the increase in the evaporation driving force. This thin and dry outer phase therefore shields the systems from humidity variations. Such a feedback loop achieves a homeostatic regulation of water evaporation.

homeostatic | evaporation | self-assembly | gradient | regulation

The evaporation of water from an aqueous medium to a dry gas phase is a ubiquitous phenomenon in nature. Evaporation can occur freely, as from oceans into the air, or be hindered by membranes or barrier films. Land-living organisms face the challenge of adjusting to the relative humidity (RH) of ambient air, which varies from a few percent to saturation at 100%, whereas the living-cell water chemical potential corresponds to a RH of above 99%. This difference drives water transport from the cells to the ambient air, exposing life to a drying-out threat. Different strategies have emerged to counter this threat. Plant leaves are covered with a waxy cuticle layer composed of polymers and associated lipids (1), whereas animals like mammals are protected by a skin composed of dead cells embedded in a lipid matrix (2), and a lipid film on the tear liquid of their eyes (3). Water transport across an inert diffusional barrier is proportional to the difference in water chemical potential between the inside and the outside. Total water loss through an inert membrane would thus vary in response to changes in the environmental humidity, with the risk of massive water loss in dry conditions. This phenomenon is typically observed in the plant cuticular film that coats the leaves (1, 4), as displayed in Fig. 1. On the contrary, several studies show that, for healthy human stratum corneum, the outermost layer of skin, the evaporation rate increases with lowering RH at high humidities, whereas it is virtually constant and independent of the outside humidity for RH < 85% (5–7) (Fig. 1). The stratum corneum is a thin and dry layer composed of dead keratin-filled cells embedded in a lipid multilamellar matrix, which realizes the barrier function of the skin (2). This membrane responds to drier conditions by decreasing its water permeability and can thus not be described as an inert barrier membrane. Sparr and Wennerström (8) previously pointed out a mechanism for this responsive behavior of the stratum corneum based on theoretical calculations of water fluxes through a multilayered structure of lipids (Fig. 1). The key ingredient in the model is the possibility of a phase transition in the lipid self-assembly structure at reduced water chemical potential. The ability of this simplistic model to reproduce the behavior of the real biological system suggests the existence of a common general mechanism.

Results

In this work, we demonstrate that simple binary or ternary systems can exhibit the same humidity-buffering behavior as the stratum corneum. The key is the ability of the system to form different self-assembled structures, with different transport properties, depending on the water content. This implies the existence of a feedback loop on the water loss across the interface through structural changes in the interfacial layer in response to changes in boundary conditions (9). We designed an experimental setup to study the nonequilibrium system of the air–liquid interfacial layer through the monitoring of the following: (*i*) the water loss with gravimetric measurements, (*ii*) the water composition gradient with infrared microscopy, (*iii*) the sequence of phases with polarized optical microscopy, and (*iv*) the nanostructure with small-angle X-ray scattering (SAXS) profiles (Fig. 2).

The measuring cell is a flat capillary tube with a rectangular cross-section of 0.1 × 1 mm. One end is connected to a large bulk reservoir, whereas the other end is placed under a constant airflow of known RH (Fig. 3). Both boundary conditions in the capillary cell (tip and reservoir) are thus known and constant. Using this device, which was inspired from the so-called penetration experiments and microfluidics pervaporation cells (10–13), we demonstrate how nonequilibrium interfacial structures are formed at the air–liquid interface, and how these structures influence water transport. We are thus able to monitor the drying process in unprecedented detail.

We obtained experimental data for two different model systems composed of amphiphilic molecules and water that both exhibit a variety of structures depending on the water content (Fig. 2). The first system was a binary mixture of a sugar-based surfactant, α-dodecylmaltoside (DDM), and water. The second system was a ternary mixture of a sugar-based surfactant, β-octyl glucoside (OG), a lipid, 1-palmitoyl-2-oleoylphosphatidylcholine (POPC), and water. At high water contents, both systems form

Significance

Water evaporation from aqueous solutions of amphiphilic molecules is shown to be independent of the evaporation driving force, which is the air relative humidity. This reproduces the behavior observed for mammals' skin outer layer. An homeostatic mechanism achieves the control of water evaporation in systems that adapt their structure to their water content. The response to a change in relative humidity operates through a change in thickness of the self-assembled phase in contact with the air, and thus a change in permeability to water in this layer. This external layer shields the rest of the system from humidity variations and sets the hydration below this shield.

Author contributions: K.R. and E.S. designed research; K.R. and E.S. performed research; K.R., M.L., J.H., and Q.D.P. contributed new reagents/analytic tools; K.R. and E.S. analyzed data; and K.R. and E.S. wrote the paper.

The authors declare no conflict of interest.

[1]To whom correspondence should be addressed. Email: kevin.roger@ensiacet.fr.

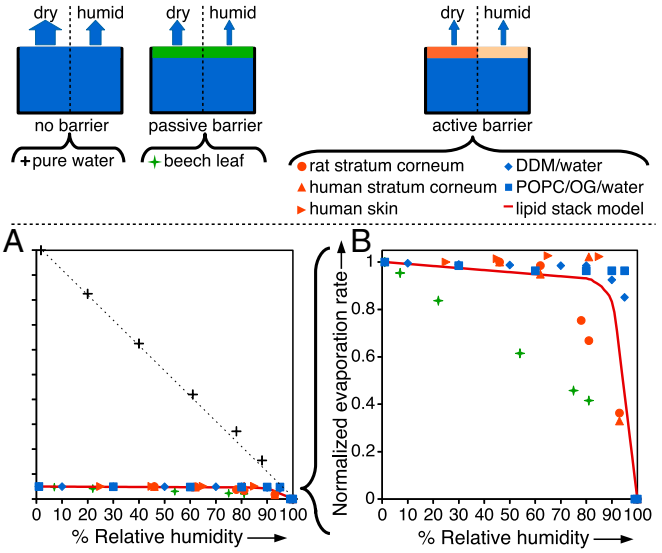

Fig. 1. Variation of the evaporation rate with the air RH for various systems, measured by a gravimetric method or taken from the literature [pure water, in vivo study of beech (*Fagus sylvatica* L.) leaf discs (4), in vitro study of rat stratum corneum (7), in vitro study of human stratum corneum (6), in vivo study of human skin (5), and DDM/water and POPC/OG/water model systems]. For each system, the evaporation rate is normalized by its value at the lowest RH of 0.5%. (*A*) In all cases (skin, leaves, and solutions of amphiphiles), the evaporation rate is reduced compared with pure water. As an example, the evaporation from the DDM/water system is 20 times slower than from pure water after 1 h of drying. (*B*) Evaporation through beech leaves depends linearly on the humidity, which is typical of a passive barrier. On the contrary, for the stratum corneum and model systems, the evaporation rate is constant over most of the RH range. The latter systems behave like responding membranes such as a stack of lipid bilayers as modeled by Sparr and Wennerström (8).

micellar solutions. These solutions are poured in the reservoir of the capillary cell and flow toward its tip through capillarity. At the tip, the solutions are exposed to an airflow of known RH and evaporation takes place. Due to the dimensions of the capillary cells, inertial forces are small compared with viscous forces, which corresponds to low Reynolds numbers and thus creeping flow. We measured the velocity of pure water in the capillary cell as 8.5×10^{-6} m·s^{-1} at RH = 0.5%. At 23°C in a 100-μm gap, this corresponds to a Reynolds number of Re $\sim 9 \times 10^{-4} \ll 1$. Aqueous solutions of amphiphiles possess larger viscosities and the formation of a barrier at the air–liquid interface reduces the flow rate, which will yield even lower Reynolds numbers. Transport therefore occurs through unidirectional advection due to the capillary flow and diffusion due to the difference in water chemical potential between the two boundaries.

First, we verified that the chosen simple systems reproduced the leveling off in the rate of water loss with decreasing humidity, as observed with the human stratum corneum (Fig. 1). This was done through gravimetric measurements of the water loss through several capillaries linked to the same reservoir, the tips of which were exposed to air of controlled RH. We monitored the mass loss in the capillaries over time, for both model systems and pure water, at different RHs (Fig. S1). For pure water, the mass loss increased linearly with time and the corresponding slope decreased linearly with increasing RH (Fig. 1*A*). If a passive barrier exists to hinder the transport, such a signature is unchanged, as shown for beech leaves (Fig. 1*B*). On the contrary, both investigated model systems displayed a nonlinear response of the water evaporation rate to the variation in RH. This implies that the resistance to the water flux in the interfacial film varies with the boundary conditions in RH, similarly to the stratum corneum (Fig. 1*B*). For both model systems, we observed that the mass loss increased approximately with the square root of time (Fig. S1). For a given time point, the mass loss was nearly independent of the RH (RH < 85% for the DDM/water system and RH < 99% for the POPC/OG/water system as displayed in Fig. 1). For each system, a time-independent evaporation rate can be defined as the slope of the linear function expressing the mass loss with time to the adequate exponent ($t^{1/2}$ for the model systems). The evaporation rates are normalized by the evaporation rate at the driest conditions RH = 0.5% to emphasize the changes with RH for the different systems.

Each time point corresponds to a given spreading of the composition gradient in the capillary. As shown throughout this manuscript, the system is at local thermodynamic equilibrium in the water gradient. The response to perturbations in local thermodynamic conditions is thus faster than the spreading of the gradient. Therefore, each phase formed in the gradient can be described as a layer of given thickness, whose response to humidity changes mimics the response of membranes of given thicknesses, such as the stratum corneum. The striking feature of Fig. 1 is that we observe a very similar signature for a complex biological system, the upper layer of skin (stratum corneum), and simple binary and ternary model systems, which suggests a common underlying mechanism. We thus studied the simple model systems to unveil the microscopic mechanism behind the macroscopic responsive behavior.

To quantify the variation in water concentration in the interfacial layer, we performed near-infrared microscopy experiments at the MAX-IV synchrotron using a spatial resolution of 20 μm. A broad band at 4,800–5,300 cm^{-1} in the spectra corresponds to the OH bend–stretch combination band of water. The integral of this peak thus quantifies the amount of water in the sample (12). We mapped out the capillary by taking a spectrum every 20 μm, which allows to calculate the water amount for each

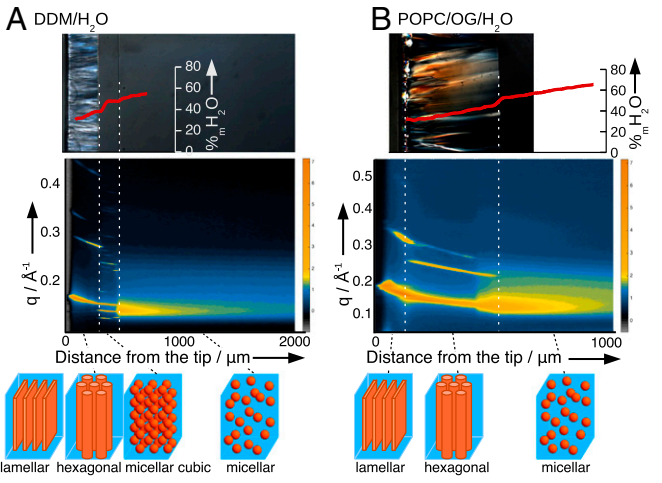

Fig. 2. Multitechnique characterization on two model systems: (*A*) DDM/water system and (*B*) POPC/OG/water system. The upper panels correspond to observation of the flat capillaries through optical microscopy using crossed polarizers. Birefringent anisotropic phases appear bright, whereas isotropic phases appear black. Phase boundaries are visible as lines parallel to the capillary edge. Superimposed with the microscopy images are quantitative data of the gradient in water content (red lines), as obtained from infrared microscopy measurements (spatial resolution, 20 μm). The middle panels show structural maps obtained through SAXS (spatial resolution, 20 μm). The color scale corresponds to the logarithm of the scattered intensity. The map displays the spatial variation of the scattering vector magnitude, *q*, which gives the structure correlation length. Bright lines correspond to structure peaks that characterize the type of self-assembly structure. The lower panels show simplified structural illustrations of the identified phases.

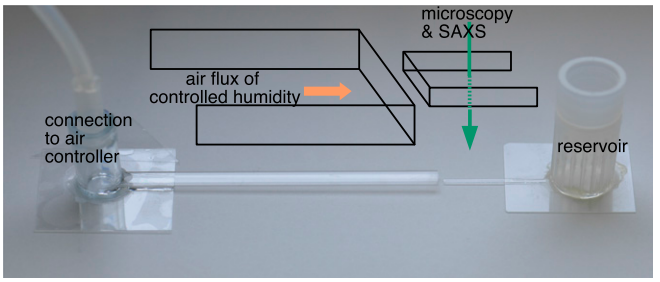

Fig. 3. Picture and scheme of the capillary setup. A small capillary is connected to a nearly infinite reservoir (*Right*). The tip of this capillary faces the tip of a larger capillary, which blows air of controlled and known humidity.

position. As displayed in Fig. 2, we can monitor the buildup of a gradient in water concentration from the tip to the inside of the capillary. This gradient is inherent to a multicomponent system placed between two boundaries of different water chemical potentials. In addition, simultaneous observation by a light microscope allowed to locate the phase boundaries. For both systems investigated, there is a stepwise change in the water concentration in addition to a gradient in swelling. The step corresponds to the change in water content associated with the transition between two phases with distinctly different compositions. We observe that the spatial location of this transition changes with time as the gradient spreads from the tip toward the reservoir, whereas the water compositions at the phase boundaries remain constant (Fig. S2). This implies local thermodynamic equilibrium in the water gradient, which can be reached because the majority of molecular degrees of freedom are in, or close to, equilibrium and respond quickly to the changes caused by dynamic nonequilibrium processes.

The gradient in water chemical potential results in a succession of different self-assembly structures. The associated phases were observed through an optical microscope using a crossed polarizer/analyzer setup, which distinguishes isotropic from anisotropic phases. The phase boundaries were observed as lines parallel to the capillary edge (Fig. 2). To monitor the nanostructure of each phase, we performed SAXS (10). Experiments were performed at the cSAXS beamline of Paul Scherrer Institut, which allows a spatial resolution of around 20 μm.

The scattering patterns showed distinct peaks, whose relative positions were characteristic of the different liquid crystalline structures (Fig. 2). We mapped out the capillary by measuring the scattering pattern every 20 μm, from which we extracted one-dimensional spectra that display the peak positions. This "SAXS-microscopy" yields structure maps (Fig. 2), with the x axis corresponding to the position in the capillary, the y axis to the q value, and thus the characteristic lengths of the structure. The color scale corresponds to the logarithm of the scattered intensity, and bright lines thus correspond to narrow structure peaks. This structural mapping was performed as a function of time and RH. For a given system and humidity, the only change with time is the spreading of the structural gradient, whereas the structure pattern is unchanged (Fig. S3). For a given system and time, humidity only affects the first spectra, which indicates that only the phase in contact with the air is influenced by the humidity boundary condition (Fig. S4). Simultaneous microscopy observations of the interfacial layer confirmed that visually observed phase boundaries coincide with distinct changes in the SAXS pattern maps. In the inner parts of the interfacial film that approaches the reservoir conditions, the sharp lines give way to a broad band, which corresponds to the loss of the liquid crystalline order in the micellar phase. A combined analysis of relative peak positions and 2D pattern symmetry allows us to determine the structure of each phase. For the DDM/water system, we observed the sequence of phases predicted from the equilibrium phase diagram (14). The system is at local thermodynamic equilibrium in the gradient. The following phases were observed with decreasing water content, from the reservoir toward the tip: micellar solution, cubic micellar phase (pm3n), hexagonal phase (p6m), and solid disordered lamellar phase (15). The outer solid phase is extremely thin and the SAXS spectra at the edge of the capillary contain both the signature of the hexagonal phase and the first order of this solid disordered lamellar phase, at a slightly higher q value than the first order of the hexagonal phase. This signature of the solid phase disappeared in more humid conditions, if RH > 85% (Figs. S4 and S5). The absence of any peak at larger scattering angles in the wide-angle X-ray scattering domain confirmed that this phase was not crystalline. For the POPC/OG/water system, a transition from micellar to hexagonal to lamellar phase was observed. In all SAXS structure maps, the bright lines, which correspond to structure peaks, are curved. This indicates a change in the characteristic distance with water chemical potential, as the structure swells with water. The observation of the 2D scattering patterns indicated a strong alignment of anisotropic structures, with rods and lamellae arranged orthogonally to the water flux (Fig. S6). An alignment orthogonal to the flux was also observed for capillaries with a circular cross-section.

The drying process was systematically studied at different relative humidities using polarized optical microscopy. The sample was observed in-between two crossed polarizers. Isotropic phases thus appear black, whereas anisotropic appear brighter depending on their orientation. We observed that the birefringence of the anisotropic phases was maximal if the polarizers were at an angle of 45° compared with the capillary, which confirms that the phases are strongly oriented in the capillary, although some defects are visible. The thickness of each phase was monitored precisely as a function of time, and the results for both systems are shown in Figs. 4 and 5. The outer phase, which is in contact with the external airflow, was the thinnest phase for all systems investigated, and its thickness increased with decreasing humidity. On the contrary, the thickness of all of the inner phases was independent of the RH at the capillary edge and increased with the square root of time, which is characteristic of diffusion-controlled processes. For the DDM/water system, the outer lamellar phase disappeared at RH = 85%. For RH > 85%, the neighboring hexagonal phase became the outer phase and its thickness then varied with RH.

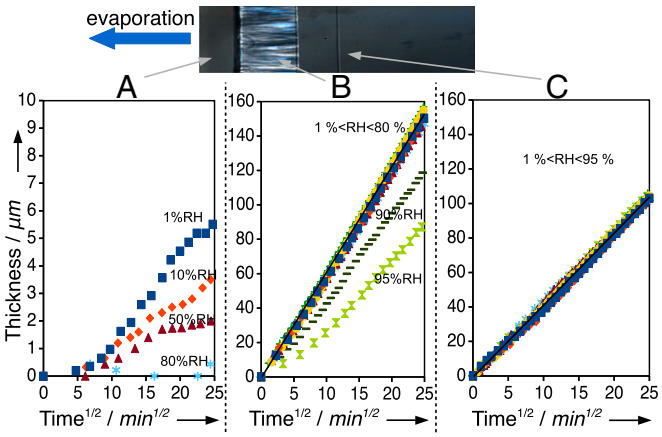

Fig. 4. The increase in thickness of different phases in the interfacial layer as a function of time, as obtained from the optical microscopy images (*Top*) (DDM/water system). The air RH varies between 0% and 95%. (*A*) The thickness of the external lamellar phase in contact with air depends on RH, and this phase disappears for RH > 85%. (*B*) The thickness of the hexagonal phase is independent of RH until the disappearance of the outer lamellar phase at RH > 85%. (*C*) The thickness of the micellar cubic phase is always independent of RH.

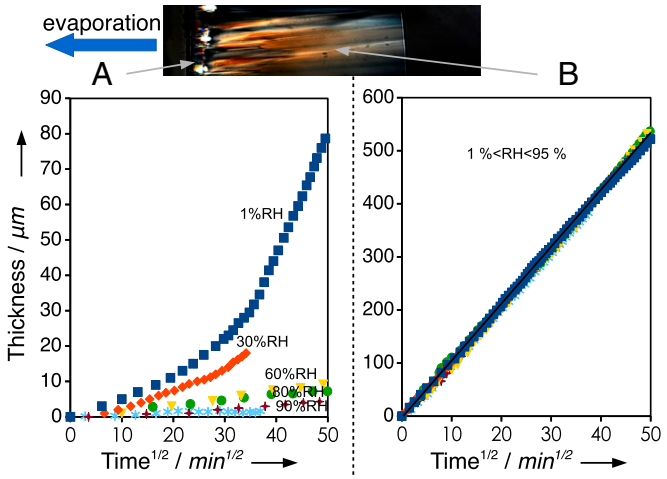

Fig. 5. The increase in thickness of different phases in the interfacial layer as a function of time, as obtained from the optical microscopy images (*Top*) (POPC/OG/water system). The air RH varies between 0% and 95%. (*A*) The thickness of the external lamellar phase in contact with air depends on RH. (*B*) The thickness of the hexagonal phase is independent of RH.

To confirm the disappearance of the outer phase at a certain RH, we performed a separate sorption calorimetry experiment. This method yields the simultaneous measures of the sorption enthalpy and the chemical potential of water for the whole hydration process (16). Of particular interest to the present work is the relationship between water chemical potential and water content. For the DDM/water system, a stepwise uptake of water was observed around RH = 85%, and was accompanied by an endothermic heat effect (Fig. S7). This is consistent with a phase transition between a lamellar and a hexagonal phase (17). We thus confirmed that the outer lamellar phase of this system was not thermodynamically stable at relative humidities above RH of 85%. The solid lamellar phase disappears at the air–liquid interface in more humid conditions, and it is then replaced by the neighboring phase in the phase diagram, which is the hexagonal phase. For the POPP/OG/water system, on the other hand, no phase transition was detected by sorption microcalorimetry at RH < 95% (Fig. S7). This is consistent with the observed independence of the thickness of the inner phase toward the RH, as this hexagonal phase is always shielded by the same outer phase (Fig. 5*B*).

Discussion

The microscopic observations of interfacial phase separation in a water gradient can now be used to understand the macroscopic evaporation rates measured through gravimetric mass loss experiments (Fig. 1). Indeed, at any given time, the total mass of evaporated water is the integral of the water mass concentration over the capillary volume:

$$m_{H_2O}^{lost} = \iiint_{V_c} c_{H_2O}^{m}(V)\mathrm{d}V, \qquad [1]$$

where $m_{H_2O}^{lost}$ is the mass of water lost through evaporation, V_c is the volume of the capillary cell, and $c_{H_2O}^{m}(V)$ is the mass concentration of water at the location V in the 3D space. This indirect method of calculating the water loss from microscopy was fully consistent with the water loss measured through gravimetry.

Consider the DDM/water system: we have shown that the air humidity only affects the outer phase, which is much thinner than the inner phases for RH < 85%. The volume integral is thus nearly independent of the humidity for RH < 85%, which also corresponds to a constant evaporation rate over the humidity range 0 < RH < 85%, as experimentally observed. For RH > 85%, the outer phase is a hexagonal phase. The thickness of this hexagonal phase is comparable to the other phases but also then depends on the humidity. The integral, and therefore the evaporation rate, thus depends on the humidity for RH > 85%, as experimentally observed. This general reasoning relates the independence of the evaporation rate over a given humidity range to the existence of a thin outer phase at the air–liquid interface over the same humidity range. In (quasi) steady-state conditions, the water flux density is the same through each phase at any time. For two phases A and B, the flux density at time t can be expressed as follows (8):

$$J(t) = \frac{p_A}{l_A(t)}\Delta a_{\text{boundary}}^{A} = \frac{p_B}{l_B(t)}\Delta a_{\text{boundary}}^{B}. \qquad [2]$$

For a given phase, p/l is the permeability, p is the permeability linear density, which is determined by the local structure, l is the thickness, and $\Delta a_{\text{boundary}}$ is the water activity difference between the two phase boundaries of the phase. As the activity difference terms are of the same order of magnitude, we can deduce that if a phase A is much thinner than a phase B, then the permeability density to water of phase A is much lower than the permeability density to water of phase B. We can thus conclude that the evaporation rate will be independent of the humidity if the outer phase at the air–liquid interface has a much lower permeability to water than the other phases.

Many amphiphiles/water systems meet this requirement of exhibiting a low permeability phase at the air–liquid interface. Indeed, most of the RH range corresponds to low water content as shown by the activity/composition isotherms (Fig. S7). At these low water contents, amphiphilic molecules will self-assemble into structures that optimize their hydration. The curvature of these surfactant films is then either extremely low, as in lamellar or bicontinuous structures, or turned toward the water in reverse topologies. The permeability to water of anisotropic structures will depend strongly on their orientation toward the water flux (18). Nonetheless, the permeability to water of all these concentrated phases will be always be lower than for pure water as all water molecules are then interacting with amphiphilic molecules.

It is useful to keep in mind that, although we studied non-equilibrium dynamics systems, the variations with the RH were the same at any given time point. After a given drying duration, we can thus consider the system as a membrane consisting of several layers of given thicknesses, which constitutes, in terms of self-assembly structure, a model for a biological system like the stratum corneum. Consider again the nonlinear relationship between the evaporation rate and humidity in Fig. 1: the main features are very similar in human stratum corneum and in our model systems. In the dryer conditions, the evaporation rate does not change significantly with increasing RH, which is not expected based on simple transport equations and an inert membrane with constant permeability. Microscopically, we now understand that RH not only constitutes the driving force for transport but also determines the structure and thickness of the interfacial layer outer phase. The outer phase adapts its thickness to the outside humidity to maintain steady-state conditions in the whole interfacial layer. This corresponds to a negligible change in the amount of water lost as the outer phase is much thinner than the inner phases. If the air becomes dryer, the driving force for water evaporation becomes larger. However, the outer phase also becomes thicker and the overall permeability to water of the membrane thus decreases (8). This constitutes a feedback loop in which the increase in the evaporation driving force is compensated by a decrease in the permeability to water (9). This mechanism is consistent with observations of

phases transitions in the stratum corneum between solid and fluid structures (8), which possess very different permeabilities (6). The only condition on the system to obtain this feedback loop is a change of structure and thus permeability upon changing the water content, which in practice requires the system to be able to swell with water. Amphiphiles and hydrophilic polymers typically meet this condition. Additionally, the same concepts also apply to self-assembly in gradients of other evaporating solvents. The interfacial structure will then depend on self-assembly and swelling in that solvent.

This subtle coupling between environmental conditions, interfacial structure, and permeability is a robust mechanism to regulate water evaporation and set a constant water chemical potential below the interfacial film, an essential property for biological systems. However, this mechanism requires the existence of a low permeability external phase. Therefore, any composition modification in the membrane may have dramatic consequences, which is possibly illustrated by several skin diseases and dry-eyes symptoms (3, 19). Our results provide a rationale to design formulations that could counteract these changes.

Furthermore, this mechanism is relevant to the control of drying processes, as for example most food and inkjet printing (20) formulations use amphiphilic molecules. The structure/transport coupling paves the way toward homogeneous coatings through drying, which requires to avoid the coffee ring effect (21). It can also provide molecular explanations to numerous observations of multilayer films at the air–liquid interfaces (22–25), with important consequences such as the reduction of water evaporation from water reservoirs (26) and the stabilization of foams through the buildup of multilayer surfactant films (27). To conclude, we have unveiled a homeostatic mechanism illustrating the moderation principle announced by Le Chatelier, which states that the system responds to a nonequilibrium perturbation by opposing it.

Materials and Methods

Materials. Milli-Q water was used for all of the experiments. The surfactants *n*-dodecyl-α-D-maltopyranoside, dodecylmaltoside (DDM), and *n*-octyl-β-D-glucopyranoside (OG), were purchased from Anatrace with a stated overall purity of 99% and a stated anomeric purity of 94% and 98%, respectively. The lipid 1-palmitoyl-2-oleoyl-*sn*-glycero-3-phosphocholine (POPC) was purchased from Avanti Polar Lipids with a stated purity of 99%. The DDM/water solution was prepared at a weight fraction in DDM of 0.15. The POPC/OG/water solution was prepared at a weight fraction in POPC of 0.035 and in OG of 0.043. Borosilicate capillaries were purchased from VitroCom.

Cell Design. The setup was composed of two main elements. The sample cell was made of a rectangular borosilicate capillary with a cross-section of 0.1×1 mm^2 and a length of a few centimeters. One end of the capillary was connected to a small plastic cylinder, which served as a reservoir. Both elements were glued on a microscope glass cover slide. The other end was opened to the air, and we ensured its edge was cleanly cut. The sample solution was placed into the reservoir and then flew to the free tip, at which point it was exposed to the air and the drying process started. The second element of this setup was made of a larger rectangular borosilicate capillary with a cross-section of 1×10 mm^2. One end was connected to an airflow of controlled humidity (see below). The other end was placed exactly in front of the smaller capillary that contained the sample. For the SAXS experiments, the reservoir was slightly modified as the X-ray beam was horizontal contrarily to the microscopy setups whose observation path were vertical (90° tilt).

Air of Controlled RH. Two setups were used to control the RH of the air blown onto the surface of the capillary cell that contained the sample. For all optical microscopy and infrared microscopy experiments, a humidity generator from HumiSys LF, InstruQuest, was used together with a humidity/temperature probe. The desired RH was achieved through the mixing of dry and water-saturated air. For the SAXS and gravimetric experiments, another setup was used for practical reasons. Dry air was bubbled in a succession of Drechsel flasks (bubbling flasks) that contained saturated salt solutions. A collection of salts can be used to access the whole RH range, which was checked by a humidity/temperature probe.

Infrared Microscopy. Near-infrared microscopy was performed at the MAX-IV synchrotron. The sample thickness limited the spatial resolution to 20 μm. Spectra were collected at different positions along one trace in the capillary from the tip toward the inside of the capillary. The step size was 10.02 μm, and the time needed for each spectra was 22 s. The total trace was 350–500 μm, and the experiment was repeated up to 70 times (up to 7 h). In-between each scan along the capillary, a reference experiment was collected from the air phase outside the capillary. The absorbance spectra were obtained from the transmission of the sample and the reference $\text{Abs} = -\log(\text{Trans}/\text{Trans}_{\text{ref}})$. A peak at 4,800–5,300 cm^{-1} corresponds to the water OH bend–stretch, and the integral of this peak quantifies the amount of water in the sample (12). A linear calibration curve was obtained from experiments with DDM/water samples with known composition (six samples with composition ranging between 0 and 36 wt% DDM), and this was used for quantification of the water gradient in the interfacial films. The MAX-IV instrument allowed simultaneous optical and infrared microscopy observations. We thus checked the agreement between the drying at the MAX-IV facility and in our laboratory by verifying the agreement between the two sets of optical microscopy observations. This made us possible to locate the phase boundaries and plot this location on the infrared spectra. A typical infrared scan line took a dozen of minutes; therefore, it does not correspond exactly to a single microscopy image. However, we verified that the shift is actually negligible over this duration.

SAXS. SAXS experiments were carried out at the X12SA (cSAXS) beamline of the Swiss Light Source, Paul Scherrer Institut. A monochromatic beam of 12.4 keV was focused to a beam size at the sample position of 20×20 μm, which corresponded to 30% of the initial intensity. The Pilatus 2M detector was placed 2.2 m behind the sample with an evacuated flight tube between the sample and the detector to minimize air scattering and X-ray absorption. The measurement capillary was placed on a two-axis scanning stage. In practice, a typical measurement duration was 0.5 s, long enough to collect high-quality signal and short enough to avoid damaging the sample. A microscopy setup allowed to switch from X-ray exposition to a conventional optical microscopy observation, which enabled us to check the location of the phase boundaries during the experiment.

Gravimetric Measurements. A Sartorius precision scales connected to a computer was used to monitor the water loss over time. We modified the standard capillary cell in the following way: nine larger capillaries (cross-section, 0.2×2 mm^2) were connected to the reservoir, with the aim of increasing the water loss and thus improve the accuracy of the gravimetric measurement. The resulting air–liquid interface was 36 times larger than for the standard cell used in all other setups (cross section, 0.01×1 mm^2). The scales were connected to a computer that monitored and stored the mass loss variation with time. The inside of the scales box was continuously flushed with a moderate airflow of controlled humidity that was measured using an independent probe. The airflow was adjusted to ensure that it did not disrupt the mass measurement.

Optical Microscopy and Image Analysis. We used a Zeiss Axioplan optical microscope. The sample was placed between crossed polarizers to distinguish isotropic (black) and birefringent (bright) phases. The absolute length scale was obtained through observations of a ruler of known length. Typical magnifications used were 5× and 10×. The capillary sample and air cells were positioned in front of one another on a glass blade that was positioned on the microscope stage. Images were typically sampled every minute using a color camera and the dedicated Zeiss software. Two sequences are shown in Movies S1 and S2. ImageJ software (NIH) was used to extract the locations of the phase boundaries for each frame. An analysis of the whole capillary was performed through pixel reslicing and subsequent averaging.

Calorimetry. Samples of DDM or OG/POPC (10–40 mg) were dried in a vacuum desiccator in the presence of molecular sieves for 24 h before use. Samples were then transferred into the calorimetric cell in a glove bag filled with dry nitrogen. Sorption measurements were conducted using a sorption calorimeter (16, 28) at 23 °C. The sorption calorimetric cell consists of two chambers: the sorption chamber, where the studied sample is placed, and the vaporization chamber, where liquid water will be injected to start the sorption. Water vaporizes and diffuses through a tube to the sorption chamber where it is absorbed by the sample. The cell is placed into a double twin microcalorimeter (29), which separately measures thermal powers released/absorbed in the two chambers. From the measured thermal powers, one can calculate the activity of water and enthalpy of mixing of water as functions of composition of the sample (16, 28). The experimental setup could be looked upon as a continuous titration of an initially dry lipid with water

vapor. The complete sorption calorimetry experiment in the present study took ~10–14 d.

ACKNOWLEDGMENTS. We thank Håkan Wennerström for insightful discussions, Bernard Cabane for a discussion on Hele-Shaw cells, Christoffer Åberg and Gwen Christiansen for feedback on this manuscript, and Benjamin Lalanne and Emmanuel Cid for support in the Matlab analysis. We thank the MAX-IV Laboratory and Paul Scherrer Institut for funding beam time and support. The research leading to these results has received funding from the European Community's Seventh Framework Programme (FP7/2007-2013) under Grant Agreement 262348 (European Soft Matter Infrastructure). The Swedish Research Council is gratefully acknowledged for financial support both through regular grants and the Linnaeus Center of Excellence "Organizing Molecular Matter" (by E.S.).

1. Schreiber L, et al. (2001) Effect of humidity on cuticular water permeability of isolated cuticular membranes and leaf disks. *Planta* 214(2):274–282.
2. Elias PM, Friend DS (1975) The permeability barrier in mammalian epidermis. *J Cell Biol* 65(1):180–191.
3. Butovich IA, Millar TJ, Ham BM (2008) Understanding and analyzing meibomian lipids—a review. *Curr Eye Res* 33(5):405–420.
4. Hoad S, Grace J, Jeffree C (1997) Humidity response of cuticular conductance of beech (*Fagus sylvatica* L.) leaf discs maintained at high relative water content. *J Exp Bot* 48(11):1969–1975.
5. Cravello B, Ferri A (2008) Relationships between skin properties and environmental parameters. *Skin Res Technol* 14(2):180–186.
6. Blank IH, Moloney J, 3rd, Emslie AG, Simon I, Apt C (1984) The diffusion of water across the stratum corneum as a function of its water content. *J Invest Dermatol* 82(2):188–194.
7. Alonso A, Meirelles NC, Yushmanov VE, Tabak M (1996) Water increases the fluidity of intercellular membranes of stratum corneum: Correlation with water permeability, elastic, and electrical resistance properties. *J Invest Dermatol* 106(5):1058–1063.
8. Sparr E, Wennerström H (2001) Responding phospholipid membranes—interplay between hydration and permeability. *Biophys J* 81(2):1014–1028.
9. Åberg C, Sparr E, Wennerström H (2013) Lipid phase behaviour under steady state conditions. *Faraday Discuss* 161:151–166, discussion 273–303.
10. Kekicheff P, Cabane B (1987) Between cylinders and bilayers: Structures of intermediate mesophases of the SDS/water system. *J Phys France* 48(9):1571–1583.
11. Leng J, Joanicot M, Ajdari A (2007) Microfluidic exploration of the phase diagram of a surfactant/water binary system. *Langmuir* 23(5):2315–2317.
12. Laughlin R, et al. (2000) Phase studies by diffusive interfacial transport using near-infrared analysis for water (DIT-NIR). *J Phys Chem B* 104(31):7354–7362.
13. Ekwall P (1937) Über die existenz und die natur der sauren seifen. *Kolloid-Zeitschrift* 80(1):77–100.
14. Auvray X, et al. (2001) Small-angle X-ray diffraction study of the thermotropic and lyotropic phases of five alkyl cyclic and acyclic disaccharides: Influence of the linkage between the hydrophilic and hydrophobic moieties. *Eur Phys J E* 4(4):489–504.
15. Ericsson CA, Ericsson LC, Kocherbitov V, Söderman O, Ulvenlund S (2005) Thermotropic phase behaviour of long-chain alkylmaltosides. *Phys Chem Chem Phys* 7(15): 2970–2977.
16. Wadsö L, Markova N (2002) A method to simultaneously determine sorption isotherms and sorption enthalpies with a double twin microcalorimeter. *Rev Sci Instrum* 73(7):2743–2754.
17. Kocherbitov V (2005) Driving forces of phase transitions in surfactant and lipid systems. *J Phys Chem B* 109(13):6430–6435.
18. Evans FD, Wennerström H (1999) *The Colloidal Domain: Where Physics, Chemistry, Biology, and Technology Meet*. Advances in Interfacial Engineering (Wiley-VCH, New York).
19. Leiske DL, et al. (2012) Molecular structure of interfacial human meibum films. *Langmuir* 28(32):11858–11865.
20. Kabalnov AWH (2009) Diffusion in evaporating solutions. *Soft Matter* 5(23): 4712–4718.
21. Kajiya T, Kobayashi W, Okuzono T, Doi M (2009) Controlling the drying and film formation processes of polymer solution droplets with addition of small amount of surfactants. *J Phys Chem B* 113(47):15460–15466.
22. Mokhtari T, et al. (2014) Controlling interfacial film formation in mixed polymer-surfactant systems by changing the vapor phase. *Langmuir* 30(33):9991–10001.
23. Thomas RK, Penfold J (2015) Multilayering of surfactant systems at the air–dilute aqueous solution interface. *Langmuir* 31(27):7440–7456.
24. Cevc G, Fenzl W, Sigl L (1990) Surface-induced X-ray reflection visualization of membrane orientation and fusion into multibilayers. *Science* 249(4973):1161–1163.
25. O'Driscoll B, et al. (2005) Thin films of polyethylenimine and alkyltrimethylammonium bromides at the air/water interface. *Macromolecules* 38(21):8785–8794.
26. Macritchie F (1969) Evaporation retarded by monolayers. *Science* 163(3870):929–931.
27. Hurcom J, et al. (2014) The interfacial structure of polymeric surfactant stabilised air-in-water foams. *Soft Matter* 10(17):3003–3008.
28. Wadsö I, Wadsö L (1997) A second generation twin double microcalorimeter. *J Therm Anal* 49(2):1045–1052.
29. Wadsö L, Markova N (2000) A double twin isothermal microcalorimeter. *Thermochim Acta* 360(2):101–107.
30. Kocherbitov V, Söderman O (2004) Glassy crystalline state and water sorption of alkyl maltosides. *Langmuir* 20(8):3056–3061.